A Quantitative Investigation of Functionalized Glazing Stacks by Atom Probe Tomography

Jacques Perrin Toinin, Constantinos Hatzoglou, Justine Voronkoff, Hervé Montigaud, Denis Guimard, Matthias Wuttig, François Vurpillot, Oana Cojocaru-mirédin

ADVANCED MATERIALS TECHNOLOGIES
www.advmattechnol.de

A Quantitative Investigation of Functionalized Glazing Stacks by Atom Probe Tomography

Jacques Perrin Toinin, Constantinos Hatzoglou, Justine Voronkoff, Hervé Montigaud, Denis Guimard, Matthias Wuttig, François Vurpillot, and Oana Cojocaru-Mirédin**

Insulating glazings used in products for the building and automotive market consist of flat glass with low-emissivity (low-E) coatings. One challenge is to increase the infrared reflectance of the glazing stack while maintaining a high transmittance. This can only be achieved if the chemical interdiffusion between the deposited layers can be controlled and characterized down to the sub-nanometer level. For that, atom probe tomography (APT) is employed in this work; technique which allows a precise quantification of the chemical interdiffusion in 3D and down to sometimes atomic level. However, the APT specimens prepared using the standard top-to-down configuration are prone to systematic fracturing due to strong differences in field evaporation between the layers involved in the glazing stack. The usage of an untypical cross-section configuration has led to improved yields, but for the latter, artifacts need to be considered and quantified. In particular, the effect of artificial layer intermixing at interfaces due to crossover is studied. It is concluded that Ni diffuses in the Ag layer via grain boundaries already in the as-deposited state. Hence, this work opens a new perspective in terms of quantification of interdiffusion at early stages, an important finding for low-E glass applications.

1. Introduction

Insulating glazings used in products for the building and automotive market consist of flat glass with low-emissivity (low-E) coatings. The main attributes of these low-E coatings are the high transparency for visible light and high heat reflectivity. One key goal is the improvement of the energetic performance of windows, that is, an increase of the infrared reflectance while maintaining a high transmittance in the visible. These coatings are realized by magnetron sputtering because this deposition technique is versatile (metal/dielectric material deposited) and compatible with the glassmaker unit (6.0×3.2 m^2) allowing the deposition of layers of hundred to a fraction of a nanometer. The coated glass obtained is often thermally post-treated at temperatures larger than glass-transition temperature T_g (600–700 °C) to suit the specific application (tempered or bent glass). However, one challenge is to maintain the energetic performance of the coated glass until the final conception steps of the product. For this purpose, analytical tools that enable monitoring of the chemical changes at sub-nanometer level are mandatory.

The low-E stack comprises several thin layers with thicknesses ranging from 1 to 30 nm, including the conductive one, because the emissivity is directly related to the resistivity according to the Hagen–Rubens relation.[1] Ag is chosen conventionally as a conductive active layer (10 nm thick) because it

J. Perrin Toinin, M. Wuttig, O. Cojocaru-Mirédin
I. Institute of Physics (IA)
RWTH Aachen University
52074, Aachen, Germany
E-mail: perrintoinin@physik.rwth-aachen.de;
cojocaru-miredin@physik.rwth-aachen.de

C. Hatzoglou
Department of Materials Science and Engineering
Norwegian University of Science and Technology
Trondheim 7491, Norway

The ORCID identification number(s) for the author(s) of this article can be found under https://doi.org/10.1002/admt.202200922.

DOI: 10.1002/admt.202200922

J. Voronkoff, H. Montigaud
Surface du Verre et Interfaces (UMR 125)
CNRS/Saint-Gobain Recherche
39 quai Lucien Lefranc, Aubervilliers 93300, France

D. Guimard
Saint-Gobain Research Paris
39 quai Lucien Lefranc, Aubervilliers 93300, France

F. Vurpillot
Normandie Université
UNIROUEN
INSA Rouen
CNRS
Groupe de Physique des Matériaux
Rouen 76000, France

has the highest electrical conductivity among all metals. Hence, thicknesses of about 10 nm are a good compromise to obtain a high reflectance in the infrared and a good transmittance in the visible. The Ag films are deposited on a thin ZnO layer, which is used as a seed layer. Despite the non-negligible lattice mismatch of Ag with respect to ZnO (–11%), the Ag layer is stabilized by epitaxy on the basal surface of ZnO wurtzite.[2,3] A second ZnO layer is usually deposited onto the Ag layer and the resulting ZnO–Ag–ZnO sandwich is embedded by dielectric layers in order to optimize the optical performances (light transmission) and to protect the Ag layer against corrosion (from the atmosphere and the glass substrate). Moreover, adding a very thin NiCr blocker layer (usually about 1 nm thick) at the ZnO/Ag interface improves the adhesion at this interface and protects the Ag layer from oxidation by the getter effect.[4] This getter effect is important not only during the deposition process, in particular if the layer deposited on the Ag is composed of an oxide, but also during post-treatment.

During thermal post-treatments, such as tempering and bending, the composition of the stack is modified by interdiffusion reaction,[5,6] as well as by possible dewetting of the metallic layers,[7–11] affecting the desired optical and mechanical properties.[12] The polycrystalline character of some layers (Ag, ZnO, NiCr) possibly intensifies these phenomena due to the presence of internal interfaces such as heterointerfaces and grain boundaries. Hence, it is necessary to characterize them very locally, with a resolution down to a nanometer in all three dimensions. Unfortunately, the conventional characterization tools, such as X-ray diffraction (XRD), secondary ion mass spectrometry (SIMS), transmission electron microscopy (TEM), and energy dispersive X-ray spectroscopy (EDX), are very often not suitable to measure such phenomena locally (especially at the internal interfaces) due to their reduced spatial resolution, their poor detection sensitivity, and their low 3D capability at the atomic scale.[13]

Therefore, in the present work, atom probe tomography (APT) is applied to characterize the layers and their corresponding heterointerfaces within the Si(100)/SiN_x/ZnO/Ag/NiCr/ZnO/SiN_x/Si stack, which corresponds to a low-E glazing stack slightly adapted for APT analysis. APT allows a 3D chemical analysis at the atomic level of a large class of materials ranging from insulators to metals.[14–17] This technique has been widely used in the field of material science to study interdiffusion phenomena observed for multilayer components within electronic[18–22] and energy[23–28] devices. However, quantitative studies on materials with heterogeneous structure composed of both metals and insulators remains challenging.[29–31]

The purpose of this study is to explore the possibilities offered by APT for the study of glazing stacks used in the glass and coating industry. Preparation and acquisition protocols are presented and evaluated in terms of success rates and the quality of data achieved. The discrepancies and limitations of the analysis obtained are discussed. This work has implications not only for the field of functionalized glazings but more generally for the analysis of complex thin layer stacks, such as complex interlayer dielectrics (ILDs), in an integrated circuit.

2. Experimental Section

The samples were prepared in a lab-scale multi-chamber coater including several 10×40 cm^2 targets with magnetrons activated by dc or rf power discharge. The layer thickness was adjusted by the power applied and the scrolling speed of the substrate in front of the activated target. The substrate used for these depositions was silicon wafer Si (100) placed on 4 mm thick Float glass used as a sample holder. The base pressure of the deposition chamber was 10^{-6} mbar. The global structure of the stacks studied was the following: Si(100)/SiN_x/ZnO/Ag/NiCr/ZnO/SiN_x/Si. Nitride layers were deposited by reactive sputtering from an Al-doped Si target using an Ar/N_2 gas mixture to obtain a thickness of 20 nm. Zinc oxide was deposited from a ceramic Al-doped zinc oxide activated by an rf power discharge in presence of pure Ar (silicon nitride and zinc oxide Al doping will not be mentioned in the following to simplify layer description). The metal layers (Ag and NiCr) were deposited from the corresponding metal target activated in dc mode using a pure argon plasma. **Table 1** gives the layer thicknesses of the different stacks prepared and studied. First, a stack with the sequence Si(100)/SiN_x(20 nm)/ZnO(5 nm)/Ag(10 nm)/NiCr(1 nm)/ZnO(5 nm)/SiN_x(20 nm)/Si named as "reference" in Table 1 has been prepared. This sample is the closest to the stacks usually employed in the glass industry, its sheet resistance is in the same order of magnitude as in the usual industrial stacks (Table 1).

Three other sample types were prepared in which the stack structure is simplified to reduce the number of layers. For

Table 1. Summary of the glazing stacks prepared for the current study named as reference SiN20+ZnO5 and with different ZnO layer thickness named as SiN0+ZnO5, SiN0+ZnO20, and SiN0+ZnO100.

Sample name	Layer thickness [nm]				Sheet resistance [Ω/□]	Success rate [%]
	SiN_x	ZnO	Ag	NiCr		
Reference: SiN20+ZnO5	20	5	10	1	6.5	15
SiN0+ZnO5[a)]	0	5	10	1	7.9	20
SiN0+ZnO20	0	20	10	1	7	40
SiN0+ZnO100	0	100	10	1	-	70

[a)]Si:Al layer is added under the Ag layer in order to keep the stack symmetric regarding the Si:Al top layer. The success rate (in %) or yield in APT is given as well for each sample. These values were obtained only for APT tips prepared using the cross-section configuration, since, except for the SiN0+ZnO100 stack (10% yield), the APT tips prepared using the top-to-down configuration exhibited a 0% yield.

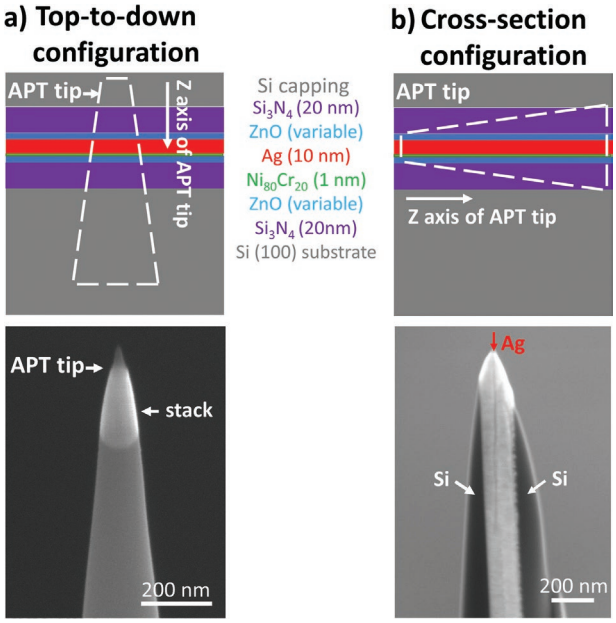

Figure 1. Schematic of the two configurations employed: a) top-to-down and b) cross-section configuration. The corresponding scanning electron microscope images showing the orientation of the glazing stack within the APT needle-shaped specimen are also given. For the cross-section configuration, the position of the Ag layer is clearly visible and indicated by a red-colored arrow.

this purpose, two samples without a dielectric layer (SiN_x) and with thick ZnO layers (100 and 20 nm) were prepared, as well as one sample with a thin layer of ZnO without a dielectric layer.

Finally, the sample surface with stacks is coated by a 100 nm Si:Al amorphous layer (deposited by dc magnetron sputtering from Al-doped Si target in the presence of pure argon) as a top protective layer before preparation for APT analysis.

APT tip-shaped specimens were prepared using the lift-out method with a dual-beam focused ion beam (FIB), FEI Helios Nanolab 600i. As shown in **Figure 1**, two different configurations were prepared, that is, the top-to-down and cross-section configuration. For the top-to-down configuration (Figure 1a), the glazing stack is placed perpendicular to the *z*-axis of the tip-shape specimen, whereas for the cross-section configuration (Figure 1b), this is placed along the *z*-axis of the tip. The advantages and disadvantages of both tip configurations and the consequences on the APT results will be discussed below.

The top-to-down configuration corresponds to the conventional lift-out technique,[32] where a wedge-shaped lamella is extracted directly from the wafer and attached to several Si microposts. The chunks obtained are then successively annularly milled using Ga^+ ions up to needle-shape specimens (or tips) are obtained with a minimum radius of ≈25 nm. This configuration allows us to analyze each layer with its best evaporation conditions since the applied field can be adjusted for each layer during the APT experiment. However, compared with other studies,[33,34] there are two main drawbacks when using this configuration: i) the high variability in analysis conditions when going from one layer to the other one decreases the spatial resolution at the interface;[35,36] ii) the high resistivity of SiN_x layers increases the fracture probability during the APT experiments.[37] It is important to mention here that this configuration could have been used only for glazing stacks with very thick ZnO layers (100 nm), and not for those with thinner ZnO layers (5 and 20 nm), since tip fracture was systematically observed during the APT experiments.

The cross-section configuration was performed using the procedure developed by Cojocaru-Mirédin et al.[38] and already applied in many material systems.[39–41] For this procedure, a molybdenum grid is needed. This Mo grid is cut into two pieces and the posts obtained are sharpened by electropolishing using a NaOH solution (5 mmol L^{-1}) (see Figure S1a, Supporting Information). Using the FIB capabilities, a wedge-shaped lamella protected by a layer of platinum is extracted from the sample and attached to these Mo posts displayed horizontally (see Figure S1b, Supporting Information). The grid is then turned vertically, and the tips are conventionally annularly milled by keeping the region of interest in the center (Figure 1b, the Ag layer is found exactly in the center of the APT tip). The main advantage of this configuration is that the probability of tip fracture during APT experiments is strongly reduced, making it possible to investigate glazing stacks with a thin ZnO layer (5 and 20 nm). The analyzed volume of the layer of interest is also strongly increased as the Ag layer remains centered in the tip during the entire analysis. The reduced tip fracture probability is explained by the fact that all the layers are evaporated at the same time implying no variation of field-evaporation parameters during APT analysis, and thus, decreasing the risk of fracture. Moreover, Table 1 shows that the reference sample SiN20+ZnO5, which contains the SiN_x layer, is characterized by the highest inhomogeneity, which explains the low success probability even though six tips were analyzed. The success rate or yield is defined here as the ratio between the number of tips successfully analyzed and the number of tips prepared in total. For the other samples, the success rate increases with increasing the thickness of the ZnO layer (as given in Table 1).

The APT experiments were performed using a Cameca local-electrode atom-probe (LEAP) 4000X-Si system with a UV (wavelength of 355 nm) laser employing ps pulses. The experimental conditions were: specimen temperature of ≈50 K, pulse repetition rate of 200 kHz, and detection rate of 0.5%. A laser energy of 17 pJ was chosen, which is favorable to evaporate Ag, but too high to obtain the correct stoichiometry of the ZnO layer. We typically have a loss of O of about 20 at.%. As suggested by many previous studies,[42–45] this loss in O is due to the formation of O-neutral species. Since the field applied on the tip-shape specimen is too low (requiring a too high laser energy), these neutral species are not field ionized, and therefore, remain undetected.[43,46] Thus, a very low laser energy of 0.5 pJ (and therefore, a higher electric field) will be ideal to obtain a stoichiometric ZnO compound, but insufficient to obtain the correct Ag layer composition. Yet, in the present study, we chose to work with a laser energy of 17 pJ, since Ag is the main layer of interest. The 3D reconstructions were obtained with Cameca IVAS 3.8.0 software using a field evaporation of 24 V nm^{-1}, a geometric field factor Kf of 3.30, and an image compression factor ICF of 1.65. These 3D reconstructions were density corrected in the *x* and *y* directions.[47] This method

makes it possible to homogenize the density in the *x*–*y* plane, and thus, to reduce the strong density variations observed in the 3D map due to local magnification effects (LME)[48] (i.e., the Ag layer with the lowest field evaporation shows the highest density in the 3D map). This density correction method allows to obtain the correct thickness of the different layers as measured by high-resolution SEM (Table S1, Supporting Information) or TEM (not shown here).

3. Results and Discussion

3.1. Difficulties Encountered when Analyzing the Glazing Stacks

One of the first difficulties encountered when analyzing the glazing stacks using the cross-section configuration is to obtain a reliable composition of the layers measured; especially of the Ag layer. **Figure 2** illustrates the analysis of the reference sample (SiN20+ZnO5) and the corresponding proximity histogram made from two 5 at.% Ag iso-surfaces from either side of the Ag layer (Figure 2c). In this APT map, the Ag layer is not centered but deviates to the right. Although the Ni/Cr composition ratio (Ni measured = 19.8 at.%; Cr measured = 5.6 at.%, i.e., Cr/Ni = 3.5) is close to the expected nominal ratio of 4, N is not detected in SiN_x layers. We clearly see a profile asymmetry between the two ZnO layers accompanied by a lower Ag content measured in the Ag layer. This profile asymmetry and the low Ag content do not correspond to the known characteristics of such a stack and are considered to be artifacts caused by the Ag layer, which is not centered in the APT tip. This clearly proves the necessity of controlling the sample preparation very well by placing the Ag layer in the exact middle position of the APT tip as illustrated in Figure 1b.

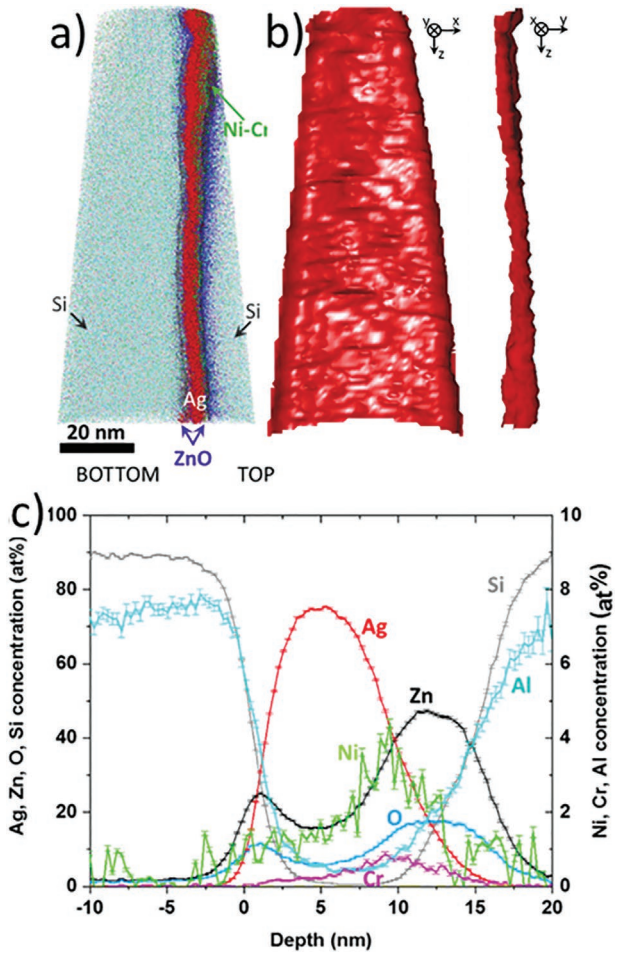

Figure 2. Analysis of the sample SiN20+ZnO5 with a non-centered Ag layer within the APT tip. a) Side view of the reconstructed volume, b) front and side view of 5 at% Ag iso-surface, and c) proximity histogram through the layers made from two Ag iso-surfaces (5 at%).

Another example is shown in **Figure 3**. In this case, the Ag layer is well centered within the APT tip, but the Ag layer is tilted by 9°. Moreover, the maximum Ag composition of 65 at.% is much lower than the 75 at.% measured in Figure 2. This suggests that tilting has an impact on the Ag composition in the Ag layer, and hence, on the entire composition of the glazing stack.

To better assess the effect of the Ag layer tilt on the Ag composition in the glazing stack, various APT tips were prepared, where the Ag layer was tilted between 0° and 20°. **Figure 4** shows that the maximum Ag composition in the Ag layer strongly varies as a function of the tilt angle (angle between the stack and *z*-axis of the APT tip): from 79 at.% for 0° to 55 at.% for 15°. One needs to mention here that this strong variation in the maximum of the Ag composition was observed especially for the glazing stacks with very thin ZnO layers (SiN20+ZnO5 and SiN0+ZnO5 samples). For the stack with a thicker ZnO layer (SiN0+ZnO20), the maximum Ag composition varies only very little around 90 at.% with changing the tilt angle. No important variation can be measured as a function of the angle of analysis or stack position. These values are comparable with the 96 at.% Ag composition measured for the Ag layer under top-to-down configuration.

It has been shown that the hemispherical shape approximation used to reconstruct the APT 3D volume can lead to artifacts in the case of samples containing materials with strong differences in field evaporations.[49–51] In fact, the tip shape becomes asymmetric because part of the tip with the lowest field evaporation becomes flat,[52] while the other part of the tip with the highest field evaporation maintains its original shape. In case the layer with the lowest field evaporation is sandwiched between two layers with high field evaporation (as in the case of an Ag layer between two ZnO layers for the cross-section configuration), the ion trajectories overlap especially in the interfacial region (due to LME,[48] i.e., the presence of layers characterized by very different field evaporations). Yet, it is difficult to estimate the reasons for the increased overlap of the layers in the case where the low field layer forms a tilt angle with the tip axis (*z*-axis). Nevertheless, it has been shown for multilayers that the most common artifact is the variation in layer thickness as a function of the analysis angle; and the layer thickness is at its maximum extent if the layers are aligned parallel to the tip axis.[53] Unfortunately, such an effect could not be observed clearly in this work. Yet, it could possibly explain the Ag composition variation with tilt angle.

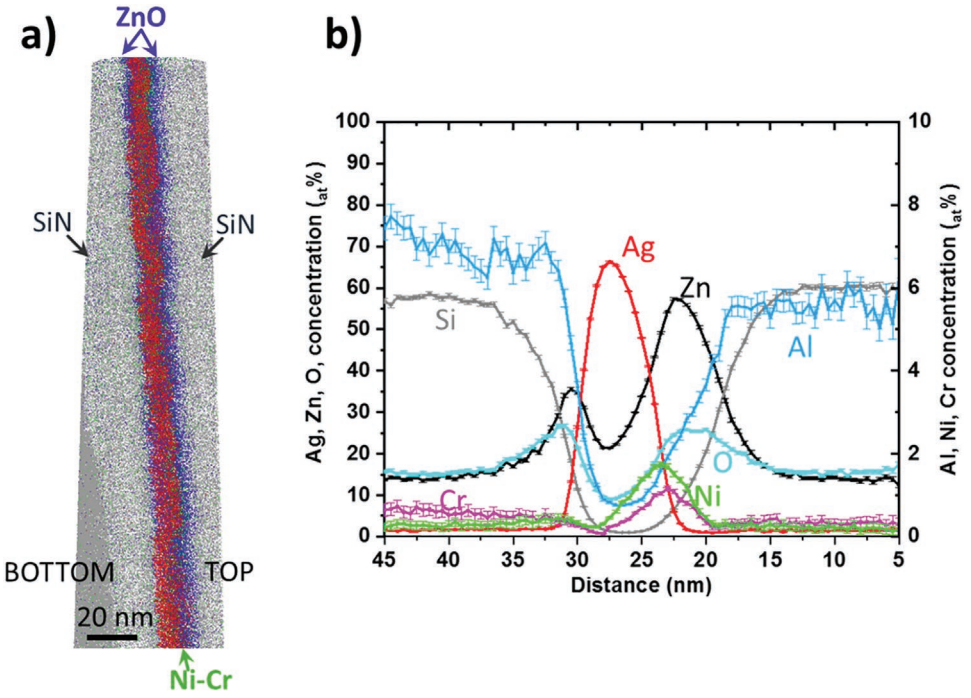

Figure 3. APT 3D map of the SiN20+ZnO5 sample where the Ag layer is tilted by an angle of 9°. a) Side view of the reconstructed volume and b) 1D composition profile constructed perpendicular to the Ag layer.

3.2. Atomic-Density Variations upon Field-Evaporation Variations as well as Field-Evaporation and Temperature Gradients

It becomes clear that another difficulty when analyzing the glazing stacks is to keep a homogenous evaporation behavior when the layers involved are very different in nature, that is, metallic, semiconducting, or even insulating. Due to large contrasts in the field evaporation generated by the stack of layers of different nature, the tip surface might undergo LME seen as a variation in atomic density on the detector event histogram. This effect is well known for 2D defects such as grain boundaries.[54,55] If these LMEs are very intense, strong intermixing between neighboring layers is encountered due to a crossover of ion trajectories.[52,56] The theoretical field evaporation of ZnO, Ag, and almost pure Ni layers involved in our glazing-type stacks is displayed in **Table 2**. The percentage of deviation in field evaporation between ZnO and Ag and between Ag and Ni are 15% and 45%, which suggests that an LME and crossover effects at ZnO/Ag and Ag/Ni(Cr) cannot be completely neglected, and hence, a strong variation in atomic density is expected.

Figure 5 presents the 3D APT map of the as-deposited sample named SiN20+ZnO5 and the corresponding proximity histogram made from two 5 at.% Ag iso-surfaces proximity histograms from either side of the Ag layer, allowing to obtain the same composition resolution at both interfaces. Hence, the composition of the whole stack, that is, from the Si wafer to the Si protection cap, can be observed from this analysis (Figure 5a,c).

Without density correction, the thicknesses of ZnO and Ag layers are ≈24 and 8 nm, which differs from the expected nominal thickness of 20 and 10 nm. The measured thickness of the Ni layer is 5 nm, which is much larger than the nominal thickness of 1 nm due to maybe possible overlaps between ion trajectories coming from the Ag and ZnO layer. Yet, the Ni composition peak is localized perfectly at the intersection region between Ag and ZnO. Moreover, the integration of the Ni and Cr profiles gives a value of 39 at.% nm for Ni and 9.9 at.% nm for Cr, which corresponds to the 80:20 stoichiometry (22.2 wt% of Cr) as expected. Finally, root mean square roughness measured for the Ag layer using a 5 at.% Ag iso-surface with a voxel size of 1 nm and a delocalization distance of 3 nm is 1.5 nm, which is of the same order of magnitude as the rms roughness of 1 nm usually obtained in this kind of stack.

The density variation between the different layers is displayed in Table 2. A correlation between density and field evaporation can be found: the density is increased for the low field-evaporation layer (Ag) while the density is reduced for the high field-evaporation layer (Ni–Cr). This suggests a high LME contribution during tip evaporation. The density correction algorithm implemented within IVAS 3.8.0 has been applied to the reconstructed tip (Figure 5d). This method allows to correct the layers' thicknesses by averaging the density in the x and y directions. The corrected values for the layer thickness are given in Table 2. Although this algorithm had provided successful results in terms of layer thickness, the overlaps between layers are amplified up to 8 nm between ZnO and Ag layers. This raises the question of whether the layer intermixing occurring during layer deposition can be disentangled from the artificial intermixing due to LME and crossover effects. Characterizing the degree of intermixing due to sputtering is indeed crucial for glazing stack applications.

In order to evaluate and quantify the LME on the evaporation behavior, simulations were performed using the mesoscopic

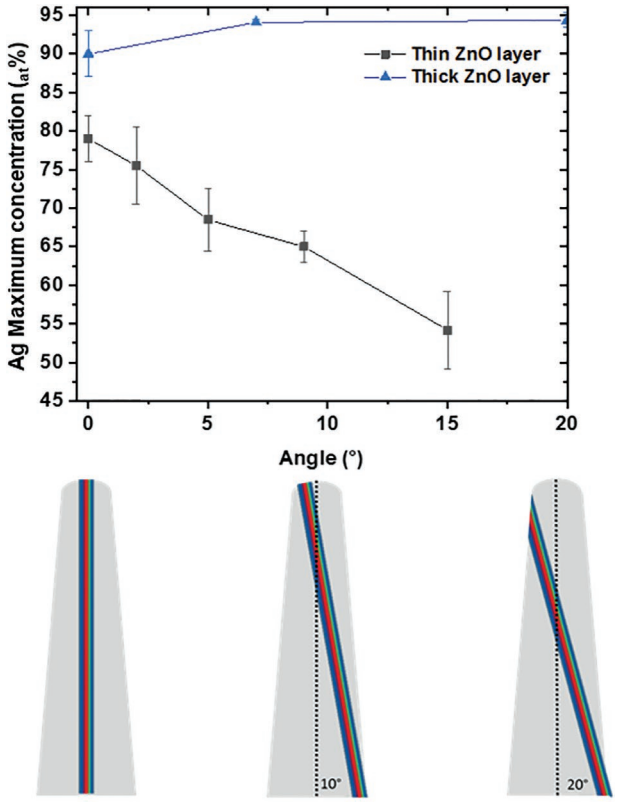

Figure 4. Maximum Ag composition measured at the center of Ag layer for various tilt angles. For thin ZnO samples (SiN0+ZnO5 and SiN20+ZnO5), the Ag composition decreases with increasing tilt angle from 0° to 15° of the Ag layer within the APT tip. Yet, it remains constant for a thick ZnO sample (SiN0+ZnO20) between 0° and 20° tilt angles. This figure is a compilation of all APT data obtained on all samples given in Table 1.

model described by Hatzoglou et al.[59] This model allowed us to estimate possible density and composition artifacts for the reconstructed volume. The stack is simulated by varying the field evaporation in a mesh in a needle-shaped specimen with a radius of curvature and shank angle corresponding to the experimental value ($R = 40$ nm and shank angle = 10°). The stack is composed of a ZnO matrix encapsulating Ag (10 nm) and NiCr (1 nm) layers. The mesh area is equal to 1 nm^2 at the apex, with an evolution along the shank. The simulations operate at a constant temperature of 50 K. The field evaporation of the NiCr layer (E_{NiCr}) has been fixed at 1.1 times the ZnO layer one (E_{ZnO}), and the Ag layer evaporation (E_{Ag}) field has been studied from 0.8 to 0.97 times E_{ZnO}. After a transformation of meshes in atoms (associating an elemental nature corresponding to the phase from which they originate) a 3D reconstruction is performed, from their positions onto the detector, using a standard hemispherical reconstruction protocol. A composition profile is finally constructed through the stack as displayed in **Figure 6**a and Figure S4, Supporting Information.

Table 2. Theoretical and experimental reduced density (ρ) measured in the analysis of the SiN20+ZnO5 sample with no-density correction, as well as layer thickness measured in no-density corrected and density corrected analysis.

ρ	ZnO	Ag	Ni
Theoretical: T	1.0	1.85	3.1
Experimental: E	1.0	2.6–4	0.7–0.8
Amplification: E/T	1.0	1.4–2.2	0.23–0.26
Theoretical field evaporation [V nm^{-1}]	28[57]	24[58]	35[58]
Layer thickness [nm]	ZnO	Ag	NiCr
No density correction	24	8	5
Density corrected	21	12	6

The theoretical field evaporation for each layer is also given. The reduced density is defined by the $V_{at,I}/V_{at,M}$ ratio, where $V_{at,M}$ is the atomic volume of the reference phase (i.e., ZnO) and $V_{at,i}$ is the atomic volume of the phase i considered.

According to the field evaporation of the Ag layer, we can distinguish three different behaviors:

1. $E_{Ag} = 0.97 \times E_{ZnO}$ in Figure 6a or Figure S4a, Supporting Information, which corresponds to the highest Ag field evaporation. No composition biases are observed in the ZnO, Ag, and Ni layers, but the Ag layer is compressed to ≈7 nm and the Ni layer is dilated to ≈3 nm. This leads to a much higher relative atomic density in the Ag and a lower relative atomic density in the Ni layer than in the ZnO layer.
2. $E_{Ag} = 0.9 \times E_{ZnO}$ in Figure S4b, Supporting Information, where the field evaporation of Ag is slightly reduced as compared to Figure 6a or Figure S4a, Supporting Information. By reducing the Ag field evaporation, no composition biases are observed, but two peaks in density appear in the Ag layer close to ZnO/Ag and Ag/Ni(Cr) interfaces. The shrinkage of the Ag layer and the dilatation of the Ni layer are further enhanced compared to Figure 6a.
3. $E_{Ag} = 0.8 \times E_{ZnO}$ in Figure S4c, Supporting Information, where the field evaporation of Ag is strongly reduced. In this case, strong composition biases in Ag and Ni layers are observed, in contrast to the two situations described above. A very high and centered density peak is observed for the Ag layer while the Ni layer has migrated to the ZnO/Ag interface. This clearly describes the crossover effect, which occurs far from the tip and cannot be compensated.

By comparing the experimental results from Figure 5 with the present simulations, we can conclude that $E_{Ag} = 0.97 \times E_{ZnO}$ situation describes the experimental data best, since neither two peaks in density in the Ag layer, nor the crossover effect have been observed.

Thus, the simulation displayed in Figure 6a allows a qualitative analysis of the experimental results. However, it does not allow to reproduce quantitatively the density variations obtained in the experiment (Figure 5) such as the density asymmetry in the Ag layer and the density difference between the upper and lower ZnO layers of the stack. Indeed, only the differences in field evaporations were considered.

Deeper experimentally driven simulations have been performed for the stack ZnO/Ag/NiCr/ZnO to evaluate the effect of Ni diffusion in Ag (in line with the next section C) and of the density asymmetry induced by the laser[60–62] (Figure 6b,c).

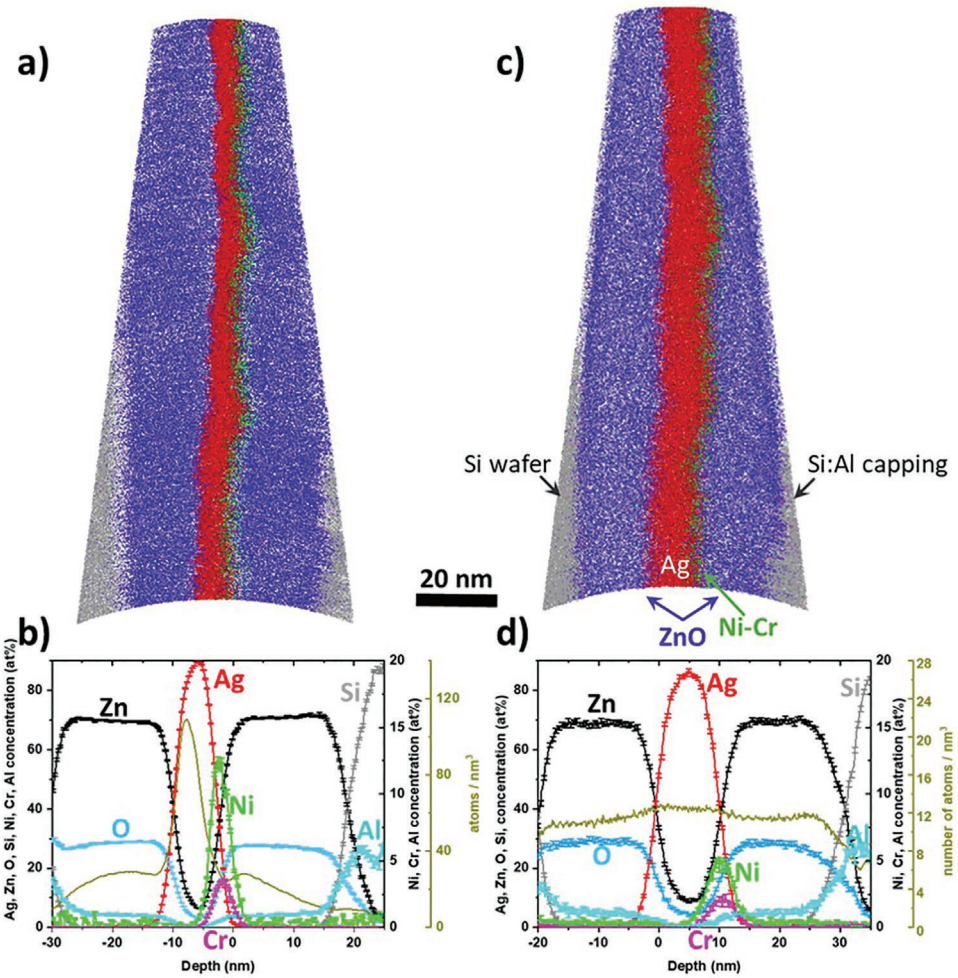

Figure 5. APT analysis of the SiN0+ZnO20 sample. a) 3D map of the cross-section view of the analyzed volumes. Si ions are displayed in grey, Ag ions in red, Ni ions in green, Zn ions in black, and O ions in blue. b) Corresponding proximity histogram computed from the 5 at.% Ag iso-surface. c,d) The 3D APT map and the corresponding proximity histogram for the APT dataset with density correction. The axis and values for the number of atoms per nm^3 are displayed in dark green.

The field evaporations used in this new simulation are close to those used in the case of Figure 6a (E_{NiCr} = 1.08 E_{ZnO} and E_{Ag} = 0.965 E_{ZnO}). On the one hand, a gradient of field evaporations starting from the NiCr/Ag interface is introduced in the Ag layer from E_{Ag} = 1.02 E_{ZnO} at the interface to E_{Ag} = 0.965 E_{ZnO} at 5 nm inside the Ag layer, simulating the diffusion of Ni inside the Ag layer (see Figure 6b). On the other hand, a temperature gradient from 150 K at the bottom ZnO layer to 50 K at the top ZnO layer has been introduced in addition to the field evaporation gradient to simulate the effect of the laser (see Figure 6c).

Only very minor notable differences in interfaces widths (see **Table 3**; simulated values) have been observed for the composition profiles from Figure 6 (in fact the interfaces widths are the biggest for the case when, besides the variation in field evaporation, gradients in field evaporation and temperature were introduced). Yet, this is not the case for the atomic density, which exhibits notable differences by varying the field evaporation and by including the field evaporation and temperature gradients (see Figure 6). The atomic density is represented in terms of the reduced density, which corresponds to the atomic density divided by the average density of the matrix (ZnO). While the density profile in the Ag layer showed a peak close to the Ag/NiCr interface and a plateau in the Ag layer (Figure 6a or Figure S4a, Supporting Information), the introduction of a field evaporation gradient, that is, a Ni composition gradient, has the effect of creating a density asymmetry in the Ag layer associated with the disappearance of the density peak at the interface (Figure 6b).

The supplementary addition of the temperature gradient introduces, besides the density changes observed in Figure 6b, a density gradient across the entire tip associated with preferential evaporation of the higher temperature zones (see Figure 6c). The corresponding 2D density maps are given in Figure S5, Supporting Information. We can conclude here that, the simulated (Figure 6c and Figure S5b, Supporting Information) and experimental (Figure 5b) profiles are in very good agreement, confirming the existence of a composition gradient in the sample and of temperature gradient during an APT experiment.

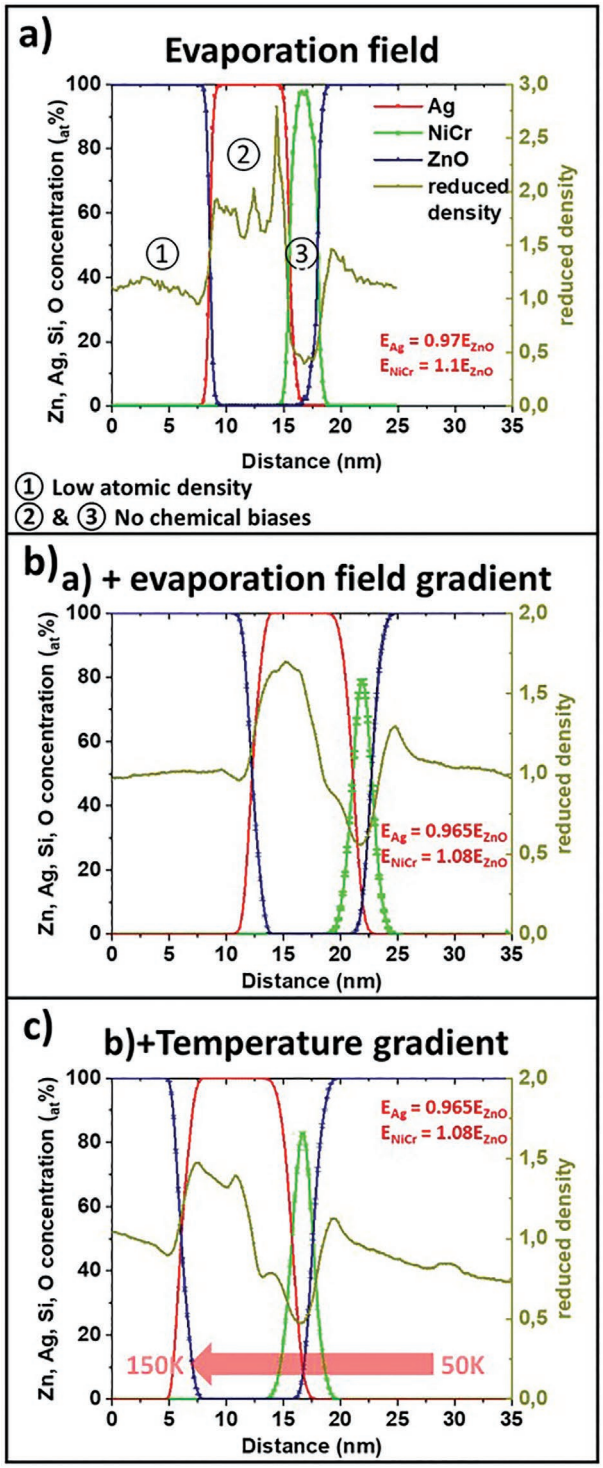

Figure 6. Atomic density and composition variations in the glazing stack upon field evaporation and temperature gradients. a) Field evaporation variation through the stack with $E_{Ag} = 0.97\ E_{ZnO}$ and $E_{NiCr} = 1.1\ E_{ZnO}$ (to be compared with Figure S4, Supporting Information). b) Simulation with a field evaporation gradient introduced inside the Ag layer next to the NiCr layer; that is, a Ni composition gradient, which mimics the Ni diffusion inside the Ag layer. c) Addition of a temperature gradient across the tip simulate the effect of the laser illumination on the needle-shaped specimen. The reduced density represents the atomic density divided by the average density of the matrix (i.e., the ZnO layer).

3.3. Application for Glazing Stacks: Determination of Layers Intermixing upon Sputter Deposition

To determine the correct value for the layer intermixing upon sputter deposition, the possible artificial intermixing (overlap between ion trajectories) due to LME needs to be first quantified. Likely, the simulations described above in Figure 6c allow us to estimate this artificial intermixing. Interestingly, the interface width is progressively increasing from ZnO/Ag to NiCr/ZnO as given in Table 3 (simulation).

The experimental values for the interface width are extracted by fitting the composition profiles using a sigmoid model as given in ref. [63] using Equation (1).

$$f(x) = \frac{c}{1 + e^{-\frac{(x_0 \pm x)}{\tau}}} + V \tag{1}$$

where V is the minimum concentration, c is the concentration difference between the base concentration and the maximum concentration, and τ is the sharpness of the profile. 4τ represents the interface width.[63] The 4τ value obtained for each interface is displayed in Table 3. As expected, the experimental values of the interface width extracted from Figure 5c are bigger than the simulated values, which suggests that true layer interdiffusion indeed takes place during sputter deposition, since $w_{LI} = w_{Exper.} - w_{Simul.}$ (where w_{LI} is the width of layer intermixing, $w_{Exper.}$ is the total width measured from experiments, and $w_{Simul.}$ is the width of the artificial intermixing due to LME). Yet, the width w_{LI} for Ag/Ni and Ni/ZnO, for example, is larger than the width w_{LI} of the ZnO/Ag interface. How can this difference be explained? Is, for example, Ni diffusion in Ag and ZnO responsible for this discrepancy in interface width?

The calculated values of 2 nm at the ZnO/Ag (corrected value in Table 3) correspond entirely to the interface intermixing due to the highly energetic sputter deposition process. More exactly, no Ag diffusion was registered inside the ZnO layer as no Ag peaks (corresponding to the isotopes ^{107}Ag and ^{109}Ag) were observed in mass spectra as presented in Figure S2, Supporting Information.

However, this does not apply to Ni. A detailed composition analysis of the Ag layer is displayed in **Figure 7**. The plots correspond to a 2D projection of the elemental compositions in

Table 3. Intermixing at ZnO/Ag, Ag/Ni, and Ni/ZnO interfaces.

Interface width		ZnO/Ag[nm]	Ag/Ni[nm]	Ni/ZnO[nm]
Experiment (4 τ)		3.4	4.4	5.2
Simulation	Figure 6a	1	1.2	1.3
	Figure 6b	1.4	1.5	1.8
	Figure 6c	1.4	1.7	2
Corrected (Experiment – Simulation)	Figure 6a	2.4	3.2	3.9
	Figure 6b	2	2.9	3.4
	Figure 6c	2	2.7	3.2

Interface width (nm) measured by simulation and experiment, as well as the corrected (Corrected = Experiment – Simulation) interface widths are given.

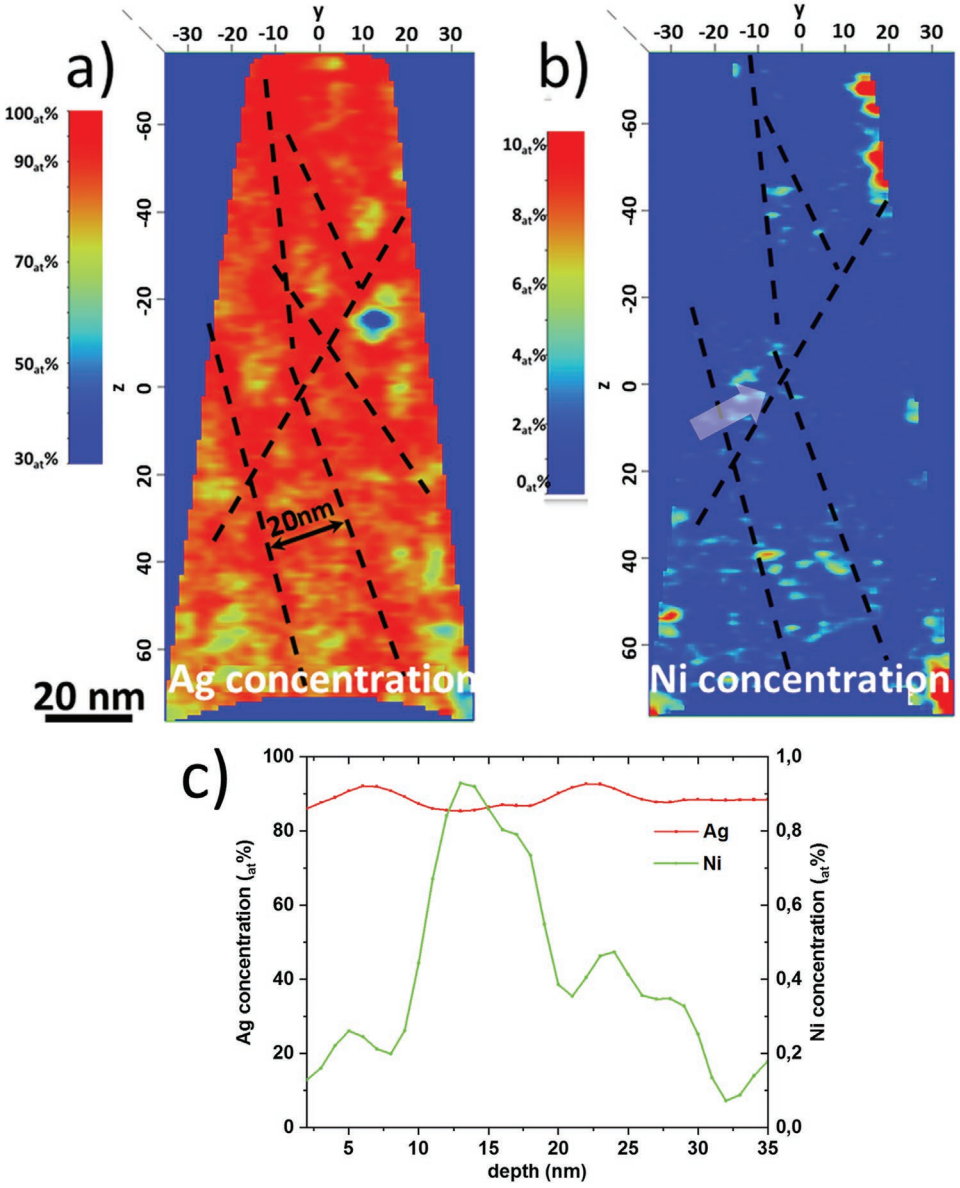

Figure 7. 2D APT composition map of a 2 nm thick slice centered in the Ag layer in SiN0+ZnO20 sample: a) Ag 2D composition map and b) Ni 2D composition map. c) 1D concentration profile built at the grain boundary marked in (b) by an arrow. This 1D concentration profile clearly proves the slight Ni enrichment at the grain boundary region.

a 2 nm thick volume centered inside the ≈10 nm thick Ag layer. In the 2D compositional map of Ag displayed in Figure 7a, we can distinguish lines of high Ag composition (>90 at.%) spaced 15 nm apart, which may be attributed to grain boundaries in agreement with Philipp.[64] These lines correspond clearly to the higher Ni composition (up to 5 at.%) regions aligned along the grain boundaries (Figure 7b). The Ni enrichment in one of the selected grain boundaries (see white arrow in Figure 7b) is even more noticeable in the 1D concentration profile from Figure 7c where Ni enrichment of up to 0.9 ± 0.1 at.% is observed. These observations allow us to conclude that Ni has already diffused inside the Ag layer in the as-deposited state via grain boundaries. This explains the wider interface width calculated at the Ag/Ni interface.

The situation is different for the Ni diffusion in ZnO. Although a very slight amount of Ni was found at a distance of 3 nm from the Ni/ZnO interface (see Figure S3a, Supporting Information; which can be explained by the large interface width of 3.2 nm as given in Table 3 for Ni/ZnO interface), clearly no Ni was found in the ZnO bulk or grain boundaries at a distance of 5 to 10 nm from the Ni/ZnO (see Figure S3b, Supporting Information). Hence, contrary to Ni in Ag, very weak Ni diffusion in ZnO was registered for the as deposited state.

This behavior of the ZnO layer as an effective diffusion barrier during deposition at high temperatures (until 600 °C) is observed for Cu(In,Ga)Se_2 thin-film solar cells.[52] Furthermore, it has been shown that Al doping of ZnO decreases the diffusivity of Ni in ZnO.[53,54] Such interdiffusion phenomena

between Ni, Ag, and ZnO should have an impact on the electrical and optical properties of the stack.[55]

Hence, this work opens a new perspective in terms of layer interdiffusion between successively deposited resistive and metallic layers. This natural phenomenon can be biased by artifacts, such as layer intermixing, due to different field evaporation, as well as strong atomic density variations due to the presence of Ni composition and temperature (from the laser) gradients.

4. Conclusions

With this work, we have proven that glazing stacks can be successfully analyzed by APT. The materials deposited for the glazing stack are characterized by a wide variety of evaporation characteristics during the analysis. On the one hand, oxides and nitrides layers are characterized by relatively high field evaporation. They, therefore, require a high electric field and low laser energy to be analyzed. On the other hand, the metallic layers are characterized by lower-field evaporation. The cross-section configuration chosen was the only way to secure a suitable success probability in APT. However, the analysis of these glazing stacks under this configuration induces various artifacts, such as LME, leading to strong deviations in density, and hence, in layer thickness, but also crossover effects which can lead to artificial layer intermixing. Moreover, very small artifacts in sample preparation, such as Ag layer off-centering as well as a tilt angle (angle between the glazing stack and the *z*-axis of the APT tip), strongly affect the measured Ag layer composition.

While the density deviations and layer thickness can be addressed using a density correction feature, the artificial layer intermixing was quantified by simulating the field evaporation of the APT tip, which embeds the glazing stack. This allows the evaluation of artificial layer intermixing at interfaces and the obtainment of the correct intermixing at interfaces during sputtering. In these simulations, laser effect and field evaporation variation inside the layers have been taken into account. Hence, we found that Ni had diffused in the Ag layer via the grain boundaries already during the sputter deposition, although no Ag or Ni was detected inside the Al-doped ZnO layers. This work opens a new perspective in terms of the quantification of interdiffusion at the early stages, which is of paramount importance for low-E glass applications.

Supporting Information

Supporting Information is available from the Wiley Online Library or from the author.

Acknowledgements

The authors gratefully acknowledge financial support of Saint Gobain (contract no 195471). O.C-M. and M.W. acknowledge the SFB 917 "Nanoswitsches" for supporting this work.

Open access funding enabled and organized by Projekt DEAL.

Conflict of Interest

The authors declare no conflict of interest.

Data Availability Statement

The data that support the findings of this study are available on request from the corresponding author. The data are not publicly available due to privacy or ethical restrictions.

Keywords

atom probe tomography, chemical intermixing, crossover effect, glazing stack, low-E coating

Received: June 7, 2022
Revised: September 8, 2022
Published online: November 7, 2022

[1] E. Hagen, H. Rubens, *Ann. Phys.* **1903**, *316*, 873.
[2] N. Jedrecy, G. Renaud, R. Lazzari, J. Jupille, *Phys. Rev. B* **2005**, *72*, 045430.
[3] N. Jedrecy, G. Renaud, R. Lazzari, J. Jupille, *Phys. Rev. B* **2005**, *72*, 195404.
[4] R. Meszaros, B. Merle, M. Wild, K. Durst, M. Göken, L. Wondraczek, *Thin Solid Films* **2012**, *520*, 7130.
[5] C. Wagner, *Acta Metall.* **1969**, *17*, 99.
[6] J. Kulczyk-Malecka, P. J. Kelly, G. West, G. C. B. Clarke, J. A. Ridealgh, *Thin Solid Films* **2011**, *520*, 1368.
[7] C. V. Thompson, *Annu. Rev. Mater. Res.* **2012**, *42*, 399.
[8] S.-L. Zhang, M. Östling, *Crit. Rev. Solid State Mater. Sci.* **2003**, *28*, 1.
[9] D. Deduytsche, C. Detavernier, R. L. Van Meirhaeghe, *J. Appl. Phys.* **2005**, *98*, 033526.
[10] C. Jahan, O. Faynot, L. Tosti, J. M. Hartmann, *J. Cryst. Growth* **2005**, *280*, 530.
[11] R. Dannenberg, E. A. Stach, J. R. Groza, B. J. Dresser, *Thin Solid Films* **2000**, *370*, 54.
[12] M. Arbab, *Thin Solid Films* **2001**, *381*, 15.
[13] S. M. Reddy, D. W. Saxey, W. D. A. Rickard, D. Fougerouse, S. D. Montalvo, R. Verberne, A. van Riessen, *Geostand. Geoanal. Res.* **2020**, *44*, 5.
[14] B. Gault, A. Chiaramonti, O. Cojocaru-Mirédin, P. Stender, R. Dubosq, C. Freysoldt, S. K. Makineni, T. Li, M. Moody, J. M. Cairney, *Nat. Rev. Methods Primers* **2021**, *1*, 52.
[15] T. F. Kelly, D. J. Larson, *Annu. Rev. Mater. Res.* **2012**, *42*, 1.
[16] F. Vurpillot, B. Gault, B. P. Geiser, D. J. Larson, *Ultramicroscopy* **2013**, *132*, 19.
[17] O. Cojocaru-Mirédin, T. Schwarz, P.-P. Choi, M. Herbig, R. Wuerz, D. Raabe, *J Visualized Exp.* **2013**, *74*, e50376.
[18] O. Cojocaru-Mirédin, H. Hollermann, A. M. Mio, A. Y.u-T. Wang, M. Wuttig, *J Phys.: Condens. Matter* **2019**, *31*, 204002.
[19] D. J. Larson, A. Cerezo, J. Juraszek, K. Hono, G. Schmitz, *MRS Bull.* **2009**, *34*, 732.
[20] P.-P. Choi, I. Povstugar, J.-P. Ahn, A. Kostka, D. Raabe, *Ultramicroscopy* **2011**, *111*, 518.
[21] A. Grenier, R. Lardé, E. Cadel, F. Vurpillot, J. Juraszek, J. Teillet, *J. Appl. Phys.* **2007**, *102*, 033912.
[22] J. H. Lee, B. H. Lee, Y. T. Kim, J. J. Kim, S. Y. Lee, K. P. Lee, C. G. Park, *Micron* **2014**, *58*, 32.

[23] P. Soni, M. Raghuwanshi, R. Wuerz, B. Berghoff, J. Knoch, D. Raabe, O. Cojocaru-Mirédin, *Sol. Energy Mater. Sol. Cells* **2019**, *195*, 367.
[24] O. Cojocaru-Mirédin, Y. Fu, A. Kostka, R. SáEz-Araoz, A. Beyer, N. Knaub, K. Volz, C.-H. Fischer, D. Raabe, *Prog. Photovoltaics* **2014**, *23*, 705.
[25] A. Koprek, P. Zabierowski, M. Pawlowski, L. Sharma, C. Freysoldt, B. Gault, R. Wuerz, O. Cojocaru-Mirédin, *Sol. Energy Mater. Sol. Cells* **2021**, *224*, 110989.
[26] O. Cojocaru-Mirédin, J. Schmieg, M. Müller, A. Weber, E. Ivers-Tiffée, D. Gerthsen, *J. Power Sources* **2022**, *539*, 231417.
[27] P.-P. Choi, O. Cojocaru-Mirédin, R. Wuerz, *Surf. Interface Anal.* **2012**, *44*, 1386.
[28] O. Cojocaru-Mirédin, M. Raghuwanshi, R. Wuerz, S. Sadewasser, *Adv. Funct. Mater.* **2021**, *31*, 2103119.
[29] K. Stiller, L. Viskari, G. Sundell, F. Liu, M. Thuvander, H.-O. AndréN, D. J. Larson, T. Prosa, D. Reinhard, *Oxid. Met.* **2013**, *79*, 227.
[30] A. D. Giddings, S. Koelling, Y. Shimizu, R. Estivill, K. Inoue, W. Vandervorst, W. K. Yeoh, *Scr. Mater.* **2018**, *148*, 82.
[31] J. G. Brons, A. A. Herzing, K. T. Henry, I. M. Anderson, G. B. Thompson, *Thin Solid Films* **2014**, *551*, 61.
[32] M. K. Miller, K. F. Russell, K. Thompson, R. Alvis, D. J. Larson, *Microsc. Microanal.* **2007**, *13*, 428.
[33] O. Cojocaru-Mirédin, P. Choi, R. Wuerz, D. Raabe, *Appl. Phys. Lett.* **2012**, *101*, 181603.
[34] O. Cojocaru-Mirédin, D. Mangelinck, D. Blavette, *J. Appl. Phys.* **2010**, *108*, 033501.
[35] D. J. Larson, T. J. Prosa, B. P. Geiser, W. F. Egelhoff, *Ultramicroscopy* **2011**, *111*, 506.
[36] S. Koelling, M. Gilbert, J. Goossens, A. Hikavyy, O. Richard, W. Vandervorst, *Appl. Phys. Lett.* **2009**, *95*, 144106.
[37] T. J. Prosa, S. Strennen, D. Olson, D. Lawrence, D. J. Larson, *Microsc. Microanal.* **2019**, *25*, 425.
[38] O. Cojocaru-Mirédin, T. Schwarz, P.-P. Choi, M. Herbig, R. Wuerz, D. Raabe, *J Visualized Exp.* **2013**, *74*, e50376.
[39] A. Stoffers, O. Cojocaru-Mirédin, W. Seifert, S. Zaefferer, S. Riepe, D. Raabe, *Prog. Photovoltaics* **2015**, *23*, 1742.
[40] M. Raghuwanshi, R. Wuerz, O. Cojocaru-Mirédin, *Adv. Funct. Mater.* **2020**, *30*, 2001046.
[41] C. H. Liebscher, A. Stoffers, M. Alam, L. Lymperakis, O. Cojocaru-Mirédin, B. Gault, J. Neugebauer, G. Dehm, C. Scheu, D. Raabe, *Phys. Rev. Lett.* **2018**, *121*, 015702.
[42] A. Devaraj, R. Colby, W. P. Hess, D. E. Perea, S. Thevuthasan, *J. Phys. Chem. Lett.* **2013**, *4*, 993.
[43] N. Amirifar, R. Lardé, E. Talbot, P. Pareige, L. Rigutti, L. Mancini, J. Houard, C. Castro, V. Sallet, E. Zehani, S. Hassani, C. Sartel, A. Ziani, X. Portier, *J. Appl. Phys.* **2015**, *118*, 215703.
[44] L. Mancini, N. Amirifar, D. Shinde, I. Blum, M. Gilbert, A. Vella, F. Vurpillot, W. Lefebvre, R. Lardé, E. Talbot, P. Pareige, X. Portier, A. Ziani, C. Davesnne, C. Durand, J. Eymery, R. Butté, J.-F. Carlin, N. Grandjean, L. Rigutti, *J. Phys. Chem. C* **2014**, *118*, 24136.
[45] M. Karahka, Y. Xia, H. J. Kreuzer, *Appl. Phys. Lett.* **2015**, *107*, 062105.
[46] D. Zanuttini, I. Blum, L. Rigutti, F. Vurpillot, J. Douady, E. Jacquet, P.-M. Anglade, B. Gervais, *Phys. Rev. A* **2017**, *95*, 061401.
[47] F. De Geuser, W. Lefebvre, F. Danoix, F. Vurpillot, B. Forbord, D. Blavette, *Surf. Interface Anal.* **2007**, *39*, 268.
[48] M. K. Miller, M. G. Hetherington, *Surf. Sci.* **1991**, *246*, 442.
[49] D. J. Larson, B. P. Geiser, T. J. Prosa, T. F. Kelly, *Microsc. Microanal.* **2012**, *18*, 953.
[50] D. J. Larson, B. P. Geiser, T. J. Prosa, S. S. A. Gerstl, D. A. Reinhard, T. F. Kelly, *J. Microsc.* **2011**, *243*, 15.
[51] N. Rolland, F. Vurpillot, S. Duguay, B. Mazumder, J. S. Speck, D. Blavette, *Microsc. Microanal.* **2017**, *23*, 247.
[52] D. Melkonyan, C. Fleischmann, L. Arnoldi, J. Demeulemeester, A. Kumar, J. Bogdanowicz, F. Vurpillot, W. Vandervorst, *Ultramicroscopy* **2017**, *179*, 100.
[53] C. Oberdorfer, G. Schmitz, *Microsc. Microanal.* **2011**, *17*, 15.
[54] S. P. Harvey, O. Cojocaru-Mirédin, in *Advanced Characterization of Thin Film Solar Cells* (Eds.: M. Al-Jassim, N. Haegel), The Institution of Engineering and Technology, London **2020**, pp. 363–387.
[55] V. Hoffmann, D. Klemm, V. Brackmann, C. Venzago, A. A. Rockett, T. Wirth, T. Nunney, C. A. Kaufmann, R. Caballero, O. Cojoccaru-Mirédin, in *Advanced Characterization Techniques for Thin Film Solar Cells* (Eds.: D. Abou-Ras, T. Kirchartz, U. Rau), Wiley, Berlin **2019**, pp. 523–568.
[56] C. Hatzoglou, B. Radiguet, F. Vurpillot, P. Pareige, *J. Nucl. Mater.* **2018**, *505*, 240.
[57] Y. Xia, M. Karahka, H. J. Kreuzer, *J. Appl. Phys.* **2015**, *118*, 025901.
[58] B. Gault, M. P. Moody, J. M. Cairney, S. P. Ringer, *Atom Probe Microscopy*, Springer Series in Materials Science, Vol. *396*, Springer, New York **2012**.
[59] C. Hatzoglou, F. Vurpillot, *Microsc. Microanal.* **2019**, *25*, 286.
[60] M. Müller, G. D. W. Smith, B. Gault, C. R. M. Grovenor, *J. Appl. Phys.* **2012**, *111*, 064908.
[61] A. Shariq, S. Mutas, K. Wedderhoff, C. Klein, H. Hortenbach, S. Teichert, P. Kücher, S. S. A. Gerstl, *Ultramicroscopy* **2009**, *109*, 472.
[62] A. Vella, *Ultramicroscopy* **2013**, *132*, 5.
[63] O. Dyck, D. N. Leonard, L. F. Edge, C. A. Jackson, E. J. Pritchett, P. W. Deelman, J. D. Poplawsky, *Adv. Mater. Interfaces* **2017**, *4*, 1700622.
[64] M. Philipp, *Electrical Transport and Scattering Mechanisms in Thin Silver Films for Thermally Insulating Glazing*, Fakultäat Mathematik und Naturwissenschaften der Technischen Universität Dresden, Université Pierre et Marie Curie, Paris **2011**, p. 71.